PHILOSOPHICAL TRANSACTIONS A

royalsocietypublishing.org/journal/rsta

Research

Cite this article: Mehmedović Z, Wei V, Grieder A, Shea P, Wood BC, Adelstein N. 2021 Impacts of vacancy-induced polarization and distortion on diffusion in solid electrolyte Li_3OCl. *Phil. Trans. R. Soc. A* **379**: 20190459. https://doi.org/10.1098/rsta.2019.0459

Accepted: 9 March 2021

One contribution of 8 to a Theo Murphy meeting issue 'Understanding fast-ion conduction in solid electrolytes'.

Subject Areas:
materials science

Keywords:
superionic, correlated motion, solid-state battery

Author for correspondence:
Nicole Adelstein
e-mail: nicoleal@sfsu.edu

Electronic supplementary material is available online at https://doi.org/10.6084/m9.figshare.c.5567420.

THE ROYAL SOCIETY PUBLISHING

Impacts of vacancy-induced polarization and distortion on diffusion in solid electrolyte Li_3OCl

Zerina Mehmedović[1,2], Vanessa Wei[2], Andrew Grieder[2], Patrick Shea[3], Brandon C. Wood[3] and Nicole Adelstein[2]

[1]Department of Chemistry, University of California, Los Angeles, Los Angeles, CA 90095, USA
[2]Department of Chemistry & Biochemistry, San Francisco State University, San Francisco, CA 94132, USA
[3]Laboratory for Energy Applications for the Future (LEAF), Lawrence Livermore National Laboratory, Livermore, CA 94550, USA

BCW, 0000-0002-1450-9719; NA, 0000-0002-7491-9592

Lithium-rich oxychloride antiperovskites are promising solid electrolytes for enabling next-generation batteries. Here, we report a comprehensive study varying Li^+ concentrations in Li_3OCl using *ab initio* molecular dynamics simulations. The simulations accurately capture the complex interactions between Li^+ vacancies (V'_{Li}), the dominant mobile species in Li_3OCl. The V'_{Li} polarize and distort the host lattice, inducing additional non-vacancy-mediated diffusion mechanisms and correlated diffusion events that reduce the activation energy barrier at concentrations as low as 1.5% V'_{Li}. Our analyses of discretized diffusion events in both space and time illustrate the critical interplay between correlated dynamics, polarization and local distortion in promoting ionic conductivity in Li_3OCl.

This article is part of the Theo Murphy meeting issue 'Understanding fast-ion conduction in solid electrolytes'.

1. Introduction

All solid-state batteries with inorganic electrolytes are a promising new technology that can replace

organic electrolytes in current Li-ion batteries. The solid inorganic electrolyte offers advances over the organic electrolyte in safety, durability, and potential volumetric and gravimetric energy density [1–8].

Nevertheless, very few solid-state batteries have been commercialized, and intensive research efforts are underway to optimize known superionic materials or discover new ones. The anti-perovskite lithium oxychloride (Li_3OCl) and the closely related hydroxychloride ($Li_{3-x}H_xOCl$) have been suggested as promising solid electrolytes, although further optimization is required [9,10]. A first step towards rationally motivated improvement of ionic conductivity is to obtain improved understanding of the diffusion mechanism. While a number of simulations of Li_3OCl have been published previously suggesting a vacancy-mediated diffusion mechanism [9,11–15], questions remain regarding the specific role of vacancy interactions, particularly at higher concentrations. In addition, previous classical molecular dynamics simulations have shown that increased vacancy concentrations lead to higher conductivities [12], but the effect of vacancy concentration on the diffusion mechanism was not explored. To augment these studies, here we report a comprehensive study varying Li^+ concentrations in Li_3OCl using *ab initio* molecular dynamics (AIMD) simulations. The AIMD simulations presented in this article reveal that the mid-range interaction between vacancies with each other and the local lattice increase diffusivity through inducing correlated and non-vacancy mediated jumps.

In addition to the previous work indicating that the primary conduction mechanism in Li_3OCl occurs through vacancy-mediated diffusion, an interstitial dumbbell knock-off mechanism has been proposed to have a lower activation energy barrier [14]. We chose to model the vacancy-mediated mechanism because Li_3OCl is thought to be Li deficient for three reasons: (i) the electrolyte likely contains some hydrogen, which substitutes for Li; (ii) Schottky pairs of Cl and Li vacancies are the lowest-energy defects and (iii) there are multiple literature suggestions that vacancies are created during synthesis, particularly at interfaces [14,16].

It is worth mentioning that lithium-rich hydroxychlorides have higher conductivities than lithium oxychloride, although unbiased experimental values are not available due to the inability to synthesize pure oxychloride without any hydrogen [9]. The enhanced conductivity in $Li_{3-x}H_xOCl$ could be caused by *both* (i) the increased concentration of vacancies and hence higher charge carrier concentration *and* (ii) correlated motion of Li diffusion events and OH rotations, as suggested in previous publications [17–20]. Analysing correlated motion in the oxyhalide is simpler than in the hydroxychloride, which is complicated by the OH rotations. In addition, we expect that qualitative conclusions regarding vacancy interactions will hold for both compounds, given the prevalence and importance of vacancies in the conduction mechanism for the two materials. Accordingly, this article focuses on the effect of V'_{Li} concentration on overall diffusivity in Li_3OCl. In a future publication, we will quantify correlated motion and the role of OH rotation in the hydroxychloride using analyses similar to those presented here.

Our results indicate that the Li vacancies, V'_{Li}, act in concert with thermal motion to distort the local lattice, which increases the jump probability compared with estimates based on carrier concentration alone. In addition, the vacancies are found to interact even at relatively dilute concentrations, inducing new jumps in their vicinity through propagation of lattice distortion and polarization of oxygen anions. Some of these jumps are found to occur via new diffusion mechanisms that bypass the dominant vacancy-mediated diffusion. Finally, we assess the effect of correlated Li motion on our reported diffusion mechanisms through a spatio-temporal analysis of jump events.

2. Methods

AIMD [21] based on density functional theory [22] were performed on a $4 \times 4 \times 4$ supercell (approx. 320 atoms) of Li_3OCl with four different Li vacancy concentrations: $Li_{2.98}OCl$, $Li_{2.97}OCl$, $Li_{2.95}OCl$ and $Li_{2.94}OCl$, using the Vienna Ab initio Simulation Package (VASP) [23,24].

Convergence tests were run with respect to the number of k-points and the planewave energy cutoff until the energy changed by no more than 10^{-6} eV. The resulting converged planewave cutoff was 400.0 eV with a Monkhorst–Pack k-point mesh of $8 \times 8 \times 8$. Plane augmented wave pseudopotentials [25,26] for Li, O, and Cl were employed with the Perdew–Burke–Ernzerhof (PBE) exchange-correlation functional [27].

The AIMD was run with Γ-only k-point sampling within the NVT ensemble with a 1 fs timestep. Simulations ran for 90–200 ps following 3 ps of thermal equilibration. The Nosé thermostat was employed and the Nosé mass 7.5 a.u. was chosen based on the phonon frequencies [11,28]. The number of Li^+ vacancies was varied from one to four, resulting in V'_{Li} concentrations of 0.5–2%. A uniform background charge was employed to compensate for each negatively charged vacancy.

The diffusion coefficient, D, for each compound was determined using the Nernst–Einstein relation based on the mean squared displacement (MSD; equation (3.2)), which was averaged across all time windows in the simulation. Uncertainty in D was calculated from the standard deviation of the diffusion coefficient after segmenting each simulation into shorter simulations of more than 20 ps each. The activation energy was calculated using the diffusion coefficients at 1100, 1200, 1300, 1400 and 1500 K. Temperatures much higher than battery operating temperatures were chosen to improve diffusion statistics based on previous AIMD simulations, which showed that a single vacancy has very little diffusion at 1000–1200 K [13]. The lattice vectors were kept at the optimized zero-temperature values, resulting in a $4 \times 4 \times 4$ supercell lattice vector of 16.08 Å.

Nudged elastic band (NEB) calculations were performed on $3 \times 3 \times 3$ supercells. Eleven images were used, and the pathway was determined using the climbing image method [29]. Further details, including an investigation of alloyed supercells, can be found in the ESM.

Analyses of diffusion events were performed using an in-house algorithm and the software package Sitator [30]. Sitator identifies Li sites and diffusion events/jumps by tracking when a Li changes site using a landmark analysis algorithm. Sitator identified 192 sites, as expected in the 320 atom supercell; the input parameters for the landmark analysis are provided in the electronic supplementary material. This algorithm does not distinguish between short-lived hops that are reversed and those that may contribute meaningfully to diffusion. Accordingly, we filtered out rapid back-hopping by introducing an additional criterion to ensure that a reverse jump between the same pair of sites has not occurred within 500 fs of the current jump. The initial locations of the vacancies in each simulation were chosen randomly. The vacancy locations were then tracked and updated by swapping indices for Li and vacancy sites whenever Li^+ jumped into vacant site. For cases in which Li^+ jumped into a site that was already registered as occupied rather than vacant, the jumps were instead classified according to the new diffusion mechanisms detailed in §3(e). Identification of diffusion events enabled the spatiotemporal correlation analysis, which was performed by recording the distance and time interval between discrete jump events, as described in the discussion section and electronic supplementary material.

Analysis was performed to determine how polarization of anions affects Li^+ diffusion. Maximally localized Wannier functions (MLWFs) [31] were used to calculate the Cl and O polarization vectors and track their interaction with V'_{Li} in both the zero temperature (NEB and static energy calculations) and AIMD simulations.

The range of interaction between vacancies was determined using a 'binding energy' calculation, in which the energy of a $4 \times 4 \times 4$ supercell with two V'_{Li} at varying distances apart was calculated. The different distances were 2.8, 4.0, 4.95, 5.6, 6.3, 7.5, 8.5, 8.9, 9.4, 9.8, 10.2 and 11.7 Å. The effect of strain relaxation was estimated by first calculating the supercell energy while freezing all the atom positions and then comparing to the supercell energy after the ions were allowed to relax until the forces on the atoms were smaller than 0.05 eV/Å, as shown in figure 2. The zero energy is set to the energy of the supercell when the vacancies are 11.7 Å apart, which is the farthest apart the vacancies can be placed in a $4 \times 4 \times 4$ supercell.

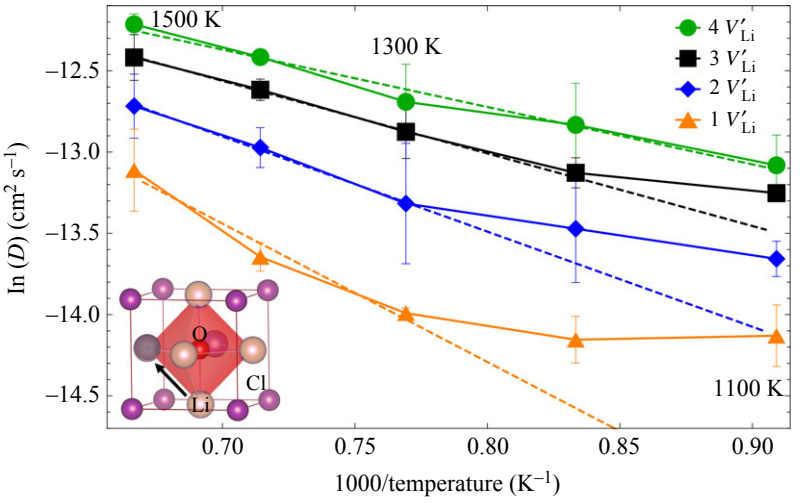

Figure 1. The Arrhenius plot of the natural log of the diffusion coefficients (D) for the four simulations with varying V'_{Li} concentrations versus inverse temperature shows variations in E_a. The inset of the unit cell indicates a Li (pink) jump to a vacant site and its octahedral cage made of 4 Cl (purple) and 2 O (red atoms). Dotted lines are guides to indicate deviations from Arrhenius behaviour that depend on vacancy concentration. (Online version in colour.)

Table 1. Diffusion coefficients (D), activation energy barriers (E_a) and maximum diffusion coefficients (D_0) extracted from linear fits of the Arrhenius plots for various concentrations of Li vacancies.

D (cm^2 s^{-1}) (T)	1100 K	1200 K	1300 K	1400 K	1500 K	E_a (eV)	D_0 (cm^2/s)
$1V'_{Li} = Li_{2.98}OCl$	7.30×10^{-7}	7.12×10^{-7}	8.39×10^{-7}	1.19×10^{-6}	2.02×10^{-6}	0.335	2.1×10^{-5}
$2V'_{Li} = Li_{2.97}OCl$	1.17×10^{-6}	1.41×10^{-6}	1.65×10^{-6}	2.32×10^{-6}	3.00×10^{-6}	0.333	3.6×10^{-5}
$3V'_{Li} = Li_{2.95}OCl$	1.76×10^{-6}	1.99×10^{-6}	2.56×10^{-6}	3.32×10^{-6}	4.05×10^{-6}	0.307	4.1×10^{-5}
$4V'_{Li} = Li_{2.94}OCl$	2.08×10^{-6}	2.67×10^{-6}	3.08×10^{-6}	4.06×10^{-6}	4.96×10^{-6}	0.304	5.0×10^{-5}

3. Results and discussion

(a) Diffusion coefficients and activation energy barriers

The Arrhenius plots of diffusion coefficients, D, versus temperature for the 1–4 V'_{Li} simulations are given in figure 1. Table 1 lists the activation energy barriers, E_a, and maximum diffusion coefficients, D_0, calculated from the Arrhenius equation: $D = D_0 * e^{-E_a/(k_B T)}$, where k_B is Boltzmann's constant and T is the temperature. The vacancy-mediated mechanism of diffusion in Li_3OCl implies that D should increase linearly with concentration $C(V'_{Li})$ in the limit of non-interacting vacancies. Instead, we found the interaction between vacancies leads to changes in E_a, which confirms that $C(V'_{Li})$ affects the diffusion mechanism.

In general, our calculated activation energy barriers are similar to other simulations. We point out that previous simulations also exhibited evidence of non-Arrhenius behaviour over a similar temperature range [12,13,32]. However, this behaviour is not universal: classical molecular dynamics at temperatures below 1000 K showed Arrhenius behaviour and little change in E_a for vacancy concentrations between 0.04 and 5% ($E_a = 0.308$ eV [12] and $E_a = 0.27 - 0.29$ eV [12,33]). We believe that the non-Arrhenius behaviour is unmistakable in our simulations for two reasons. First, unlike the classical molecular dynamics studies, we can explicitly account for polarization behaviour of the neighbouring anions to the vacancies, which we show below to play a role in

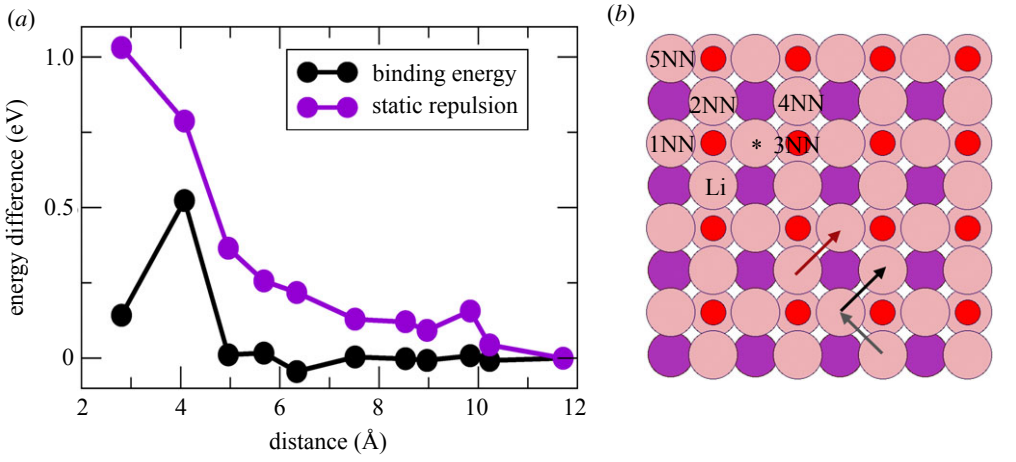

Figure 2. (*a*) The binding energy calculation shows the lattice screens the vacancies well compared to static Coulombic repulsion, *but* there is a minima out at 6.3 Å. (*b*) The simulation super-cell shows the nearest neighbour (NN) sites to an Li Wyckoff position, which can hold an Li or a vacancy. Two 1st NN correlated jumps are indicated. The red and black arrows indicate jumps in the same direction due to two different V'_{Li}, which have a jump $\cos(\theta) = 1$. The grey arrow, along with the black, indicates two jumps that could be from the same V'_{Li} (jump $\cos(\theta) = 0$). (Online version in colour.)

the diffusion. Second, our AIMD simulations are performed on comparatively large unit cells that allow for dynamical vacancy–vacancy interactions.

It is difficult to directly compare our calculated activation energy barriers to experimental measurements, which likely are of $Li_{3-x}H_xOCl$ or off-stoichiometric Li-rich antiperovskites (LRAP) [9]. NMR experiments give E_a over short diffusion distances and so can measure bulk conductivity without the effects of grain boundaries in polycrystalline LRAP, which have been calculated previously to slow diffusion [34–36] and accumulate point defects [36]. For the hydrogen containing LRAPs, E_a from NMR is 0.34–0.36 eV [9], indicating the diffusion mechanism may be similar in Li_3OCl. Nevertheless, the total diffusion coefficient in LRAPs is higher than Li_3OCl, likely because the hydrogen substitution effectively increases $C(V'_{\mathrm{Li}})$.

Figure 1 shows that the four V'_{Li} concentrations have varying deviation from Arrhenius behaviour, which increases the uncertainty in calculating E_a and D_0, especially in the 1 and 2 V'_{Li} simulations. If a linear fit is performed anyway across the range of available simulation data, the $3V'_{\mathrm{Li}}$ and $4V'_{\mathrm{Li}}$ have a lower E_a by approximately 30 meV than the 1 and 2 V'_{Li} simulations. The non-Arrhenius behaviour indicates that as temperature increases, E_a increases.

There are multiple interrelated factors that contribute to the non-Arrhenius behaviour. These can be broadly characterized as vacancy–vacancy interactions, an increase in vacancy-induced jump attempts, and additional diffusion mechanisms introduced by both temperature and vacancies. Each of these factors is discussed in detail in the subsequent sections. It is notable that the transition temperature between different slopes in figure 1, which corresponds to the onset of non-Arrhenius behaviour, decreases as $C(V'_{\mathrm{Li}})$ increases. This implies that the introduction of additional vacancies echoes the effect of elevated temperature, with both factors acting in concert to alter the diffusion mechanism.

Because the 1 V'_{Li} simulation does not have any dynamical V'_{Li}–V'_{Li} interaction effects, it can serve as a baseline for comparison. As temperature increases in this simulation, the diffusivity increases sharply following a nearly flat and slow diffusion profile between 1100 and 1300 K. Our analyses, discussed in detail below, show that local distortions induced by the vacancy increase with temperature, which in turn induces more jump events. These local distortions increase D_0 but simultaneously increase E_a (a trend that follows the so-called Meyer–Neldel rule [37]). Nevertheless, at temperatures above 1300 K, the barrier E_a in the 1 V'_{Li} simulation remains much larger than the other simulations with vacancy interactions. The increase in E_a therefore appears

to be somewhat mitigated when multiple vacancies interact. In §3b, we characterize the V'_{Li}–V'_{Li} interactions that affect diffusion.

(b) Evidence of vacancy interactions

In this section, we quantify the range and approximate energetics of the vacancy–vacancy interaction, which helps to elucidate the concentration-dependent effects on the diffusion mechanism and E_a. We do this through a vacancy 'binding energy' calculation, as described in §2. Notably, the impacts of vacancy–vacancy interactions are observable even when the vacancy concentrations are quite low (e.g. $C(V'_{Li}) = 1\%$ for the $2V'_{Li}$ case). A more comprehensive understanding of vacancy interactions from the AIMD will be presented later.

Coulombic repulsion of the negatively charged V'_{Li} predicts that on average they should maximize their distance. Instead, there is a binding energy minimum of 61 meV when the V'_{Li} are 6.3 Å apart, as shown in figure 2. We point out that a similar binding energy minimum at 6.3 Å was also reported in the electronic supplementary material of a recent publication focusing on glassy Li_3OCl [38]. Indeed, point defect clustering is common in solids because it can reduce the induced strain as long as the charge can be suitably screened. It is worth noting that this interaction energy is only slightly smaller than k_BT for the temperatures simulated (0.09–0.13 eV for 1100–1500 K), so it is reasonable to believe that the effects of vacancy interactions could be manifest in the AIMD (which we confirm in the analysis below).

A simplified explanation for the dielectric screening in ceramic oxides is that they contain highly charged ions, such as O^{2-}, that can isolate charged defects via slight lattice rearrangements. However, electrons can also participate in screening. To test for the electronic screening separate from the physical lattice polarization, we froze the atom positions and only allowed the electronic relaxation of the supercell (static repulsion). Figure 2 shows that with only electron screening, there is no 'binding energy' and the repulsive energy increases to 1 eV when the vacancies are nearest neighbours (NN), or 2.8 Å apart. Relaxing the lattice cancels much of this static repulsion, confirming that the primary stabilizing effect is local lattice restructuring. At the same time, comparing the static repulsion to the 'binding energy' simultaneously confirms the ability of the lattice to effectively screen the Coulomb interactions, while highlighting the 6–7 Å range of the effect of the vacancy on the lattice.

The relevance of local strain relaxation helps to justify the observed vacancy interaction, given that vacancies can cluster to reduce their local strain. Indeed, the binding energy at 6.7 Å only occurs after the lattice is allowed to relax (and thereby reduce the induced local strain). At finite temperature, this local strain relaxation is best described in terms of enhanced local dynamical distortion of the lattice. Because thermal effects amplify the distortion, temperature and vacancy concentration are connected, as can be seen in the non-Arrhenius conductivity trends in figure 1. A more robust quantification of the local distortion caused by vacancies, as well as its effect on increasing the probability of jump events, is presented below. We will also show that local distortion is connected to an accompanying lattice polarization effect, which manifests through the chlorine and oxygen anions.

The same signature of vacancy–vacancy interaction seen in figure 2 is also visible in the AIMD simulations, as shown in figure 3. Without the screening of the lattice, the negatively charged vacancies would maximize their distance from each other. At the other extreme, if vacancies did not interact, they would freely explore all possible sites over the simulation. In this event, the distribution of V'_{Li}–V'_{Li} distances should converge to the general distribution of Li–Li distances. As such, the V'_{Li}–V'_{Li} pair distribution function (pdf) as compared with the expected V'_{Li}–V'_{Li} pdf acts as a signature of vacancy interactions.

We find that none of the V'_{Li}–V'_{Li} pair distribution functions match the expected Li–Li pdf (figure 3), although the closest distribution is found for the $2V'_{Li}$ simulation at 1100 K. The binding energy calculation showed that although the lattice screens the charges of the vacancies relatively well, two vacancies can be trapped if they become nearest neighbours by the large 0.5 eV barrier at 4 Å (figure 2). Thus, it is reasonable to have some probability of finding two V'_{Li} as nearest

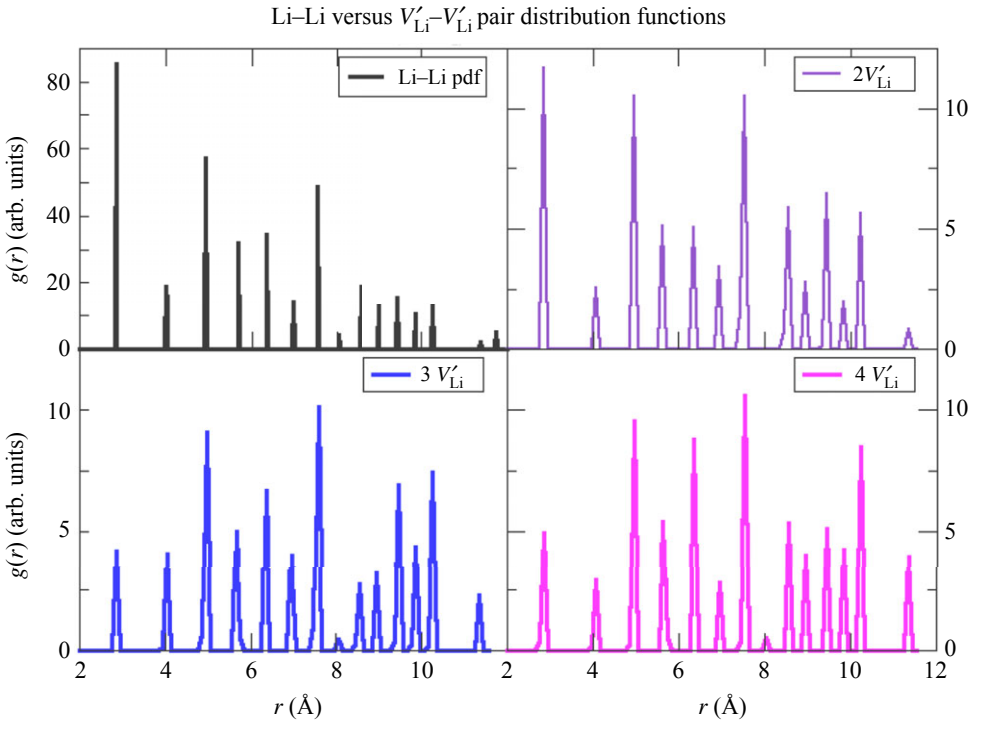

Figure 3. Vacancy–vacancy pair distribution functions (pdfs) at 1100 K demonstrate the Coulombic repulsion between the vacancies. The 2 V'_{Li} simulation has a more similar distribution to the Li–Li pdf than the higher concentrations. The $g(r)$ are in arbitrary units (arb. units). (Online version in colour.)

neighbours in the 1100 K $2V'_{Li}$ simulation, despite the apparent Coulombic repulsion. This 2 V'_{Li} pairing at 2.8 Å persists up to 1400 K, as shown in the electronic supplementary material.

In our simulation supercell, the farthest two vacancies can be from each other is around 12 Å, whereas the 'binding energy' calculation in figure 2 indicates a preferred vacancy–vacancy interaction distance of 6.3 Å. In the 3 and 4 V'_{Li} simulations, each V'_{Li} is always within this interaction distance of at least one other V'_{Li}. Indeed, we observe a decreasing ratio between peaks at 5.8 and 6.3 Å with vacancy concentration, which indicates a relatively stronger V'_{Li}–V'_{Li} interaction at 6.3 Å; this may be a signature of the local minimum seen in the binding energy calculation (figure 2). The distributions at higher temperatures, which also show a preference for 6.3 Å over 5.8 Å, are given in the electronic supplementary material. At the same time, high vacancy concentrations also favour shifts towards larger vacancy–vacancy distances because there are simply more V'_{Li} *and* they interact.

(c) Polarization effects on vacancy interactions

The mid-range effects of vacancies are communicated not only by local lattice distortion, but also by the polarization of the remaining lattice. In particular, both the oxygen and chlorine anions can be significantly polarized and interact with the diffusing species (V'_{Li}). To see this effect, we use MLWFs to calculate the polarization of each anion (§2 for details). MLWFs resemble localized molecular orbitals, and the vector sum of the four sp^3-like Wannier centres (centre of density of each MLWF) around each anion gives the polarization of the anion.

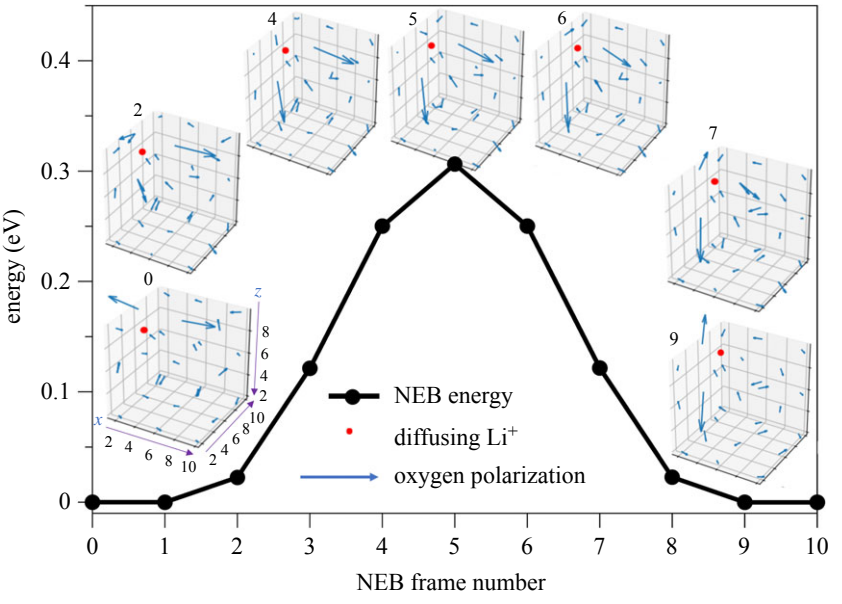

Figure 4. Three-dimensional oxygen polarizations in select frames from an NEB calculation of the activation energy barrier for a vacancy hop in a 3 × 3 × 3 supercell. The numbered plots correspond the NEB frame number and show the relative oxygen polarization (blue arrow) and the diffusing Li^+ (red) at their locations in the supercell. The *x*-, *y*- and *z*-axes of the supercell are indicated in the three-dimensional polarization plot from frame 0. As the Li^+ moves, new neighbouring oxygen ions to the V'_{Li} get polarized. (Online version in colour.)

To track the polarization of the nearby lattice during an individual diffusion event, we first ran NEB calculations of a single vacancy mobility (figure 4). Our 3 × 3 × 3 NEB calculation gave an E_a of 0.308 eV. We point out that this value is less than the 0.328 meV found for the smaller 2 × 2 × 2 cell [39], highlighting the importance of accounting for the longer-ranged effects of the lattice distortion (in contrast, prior NEB studies used 2 × 2 × 2 supercells to determine the E_a for both the vacancy-mediated and interstitial dumbbell/knock-off mechanisms [11,14,39,40]). The E_a from NEB, which has $C(V'_{Li})$= 1.23%, matches the E_a from the AIMD with $C(V'_{Li})$= 1.5 and 2%.

Figure 4 shows the polarization of the oxygen nearest neighbours across the NEB-derived minimum energy path. The two nearest neighbour oxygen anions to the vacancy are significantly more polarized than the other oxygen anions (two largest blue arrows). Moreover, the highly polarized oxygen ions (polarization vector in blue) track the vacancy as the latter diffuses between lattice sites in Li_3OCl. In figure 4, the diffusing Li^+ is indicated with the dot. As expected, the polarization vector points away from the nominal −1 charge of V'_{Li}. As the vacancy moves along the diffusion path, one of the oxygen atoms stays significantly polarized, but the other highly polarized oxygen is transferred to the new nearest oxygen neighbour.

Polarization effects are also present at higher vacancy concentrations and help to explain the observed vacancy–vacancy interaction trends. For instance, when two V'_{Li} are simulated in the binding energy calculations (figure 2), the two nearest neighbour oxygen of each V'_{Li} significantly mediate their interaction. However, when the two V'_{Li} are 4 Å away from each other (next-nearest neighbours) they share an oxygen in a linear arrangement (V'_{Li} O V'_{Li}). As such, the oxygen atom cannot screen the interaction, and the bond polarization is communicated through the complex. This leads to a penalty of over 0.5 eV in the binding energy calculation (figure 2). The corresponding oxygen polarization three-dimensional vector plots (similar to figure 4) can be found in the electronic supplementary material.

We note that significant deviations in the polarization of Br and Cl were also shown to be correlated with Li^+ diffusion events in our previous work on Li_3InBr_6 and $Li_3InBr_{6-x}Cl_x$ [41,42].

(d) Vacancy-induced local lattice distortion

In addition to electrostatics and polarization, vacancies interact with each other and with lattice ions through local distortion. In §3(b), we explored the interaction between vacancies and determined that the range of the vacancy's combined charge and local strain effects extend to a range of 6–7 Å. In this section, we quantify the local distortion based on the octahedral anion cage (Cl_4O_2) around each vacancy or Li^+ site. In the subsequent §3e, we will relate this local distortion to the appearance of new diffusion mechanisms.

The anion cage around each Li^+ forms a compressed octahedron, with longer Li–Cl bonds and shorter Li–O bonds. In the relaxed structure, this cage has a D4h symmetry with all atoms sitting at their Wyckoff positions, which forms a reference structure for the ideal shape of the coordination environment. To quantify the local distortion of each Li and V'_{Li} coordination environment from this ideal shape, we relied on the continuous symmetry measure (CSM) [43], as implemented within the SHAPE code [44]. The CSM was computed for each frame, with unitless values ranging from zero, for a perfect match to the ideal reference coordination, to much higher values for significantly distorted environments. For vacancy sites, the distortion was determined using the site centre of the empty octahedral cage, which is determined by the Sitator Landmark Analyses and is equivalent to the Wyckoff position. Note that CSM is size invariant, so isotropic contraction or expansion is neglected.

The normalized probability distributions of calculated CSM values are shown in figure 5. Figure 5*a* further separates the CSM distribution for the 1 vacancy simulation at 1100 K according to environments around vacancies (vac), first Li neighbours to vacancies (neighbour), and actively jumping Li (jump) (see electronic supplementary material for analogous plots for the other simulations temperatures and vacancy concentrations). In the latter case, a jumping Li was defined to include frames within a time window of 200 fs of the recorded discretized jump event (see §2) in order to capture any distortion that might occur before or after the jump. The breadth of the distributions is related to the softness of the Li cage with respect to thermal distortion; however, there are also clear indications of additional vacancy-induced distortions. In particular, although the vacancy sites themselves have low anisotropic distortion (presumably the distortion is instead isotropic), their presence does cause the anion cages of their Li^+ neighbours to distort. As a result, the neighbour shape distribution is shifted to higher CSM values with respect to the average. The longer tail of this distribution also likely translates to a higher probability for anharmonic distortions that are precursors to jump events. There is additional distortion from thermal oscillations, which generates increased kurtosis in the tail of all distributions.

The CSM distribution around an actively jumping Li^+ varies significantly from the total distribution, with two new peaks around 11 and 21 (see figure 5*a* inset), indicating complete loss of the octahedral coordination environment. In particular, jumping Li^+ pass through a triangular transition state geometry with one O^{2-} and two Cl^- neighbours. Notably, this analysis provides a secondary confirmation of jump detection.

Figure 5*b* compares the total CSM distributions from all simulations. It is clear that both temperature and increased vacancy concentration increase the shape distortion of Li^+ on average. This enhanced distortion is particularly strong for Li^+ neighbours to the vacancy (see electronic supplementary material). The mean shape distortion of the first main peak from each total distribution. Figure 5*c* shows that the increase in the shape distortion is roughly linear with the number of vacancies, following a similar slope for each temperature.

We hypothesize that the distortion induced in anion cages near a vacancy induce additional jump attempts, which may partially account for the increase in D_0 observed for the higher vacancy concentrations. To strengthen this connection, we computed the correlation between each degree of distortion and the corresponding distance to a vacancy *or* actively jumping Li^+. In figure 6, we compare histograms of these distances for the 1 V'_{Li} simulation at 1100 K after binning the degree of CSM shape distortions into six groups from least to most distorted (CSM ranges of 0–1.5, 1.5–3.0, 3.0–4.5, 4.5–6.7, 6.7–15.7 and 15.7–30.0). To highlight the changes in the histograms with increasing distortion, the data are presented as differences with respect to the least distorted reference (CSM 0–1.5; shown in the figure inset). A corresponding heat map of

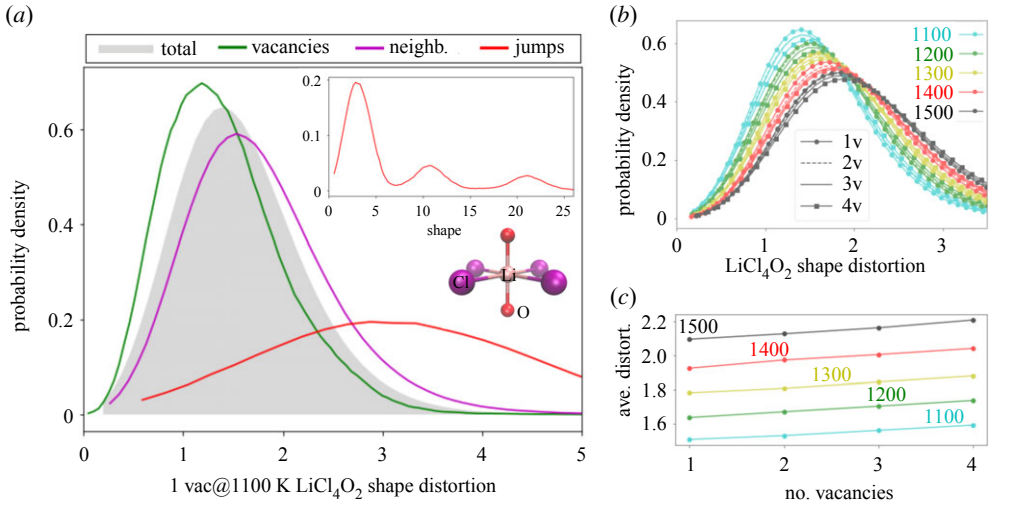

Figure 5. (*a*) Distributions of CSM values for Cl_4O_2 octahedral shapes for local environments in the 1 vacancy simulation at 1100 K, showing the shape anisotropic distortion of nearest-neighbour Li environments around a vacancy (purple neighbour), compared to the vacancy (green). The CSM distribution for jumping Li (red) shows more extreme distortions, also visible in the upper inset. The lower inset shows the ideal CSM reference $LiCl_4O_2$ octahedron. The total distribution is shown in grey. (*b*) Comparing the total shape distributions for all the simulations (five temperatures, four vacancy concentrations) shows that both vacancies and temperature increase distortions. (*c*) Quantification of the shift of the peaks plotted in *b*, given according to the mean shape distortion from the total CSM distribution in each simulation. (Online version in colour.)

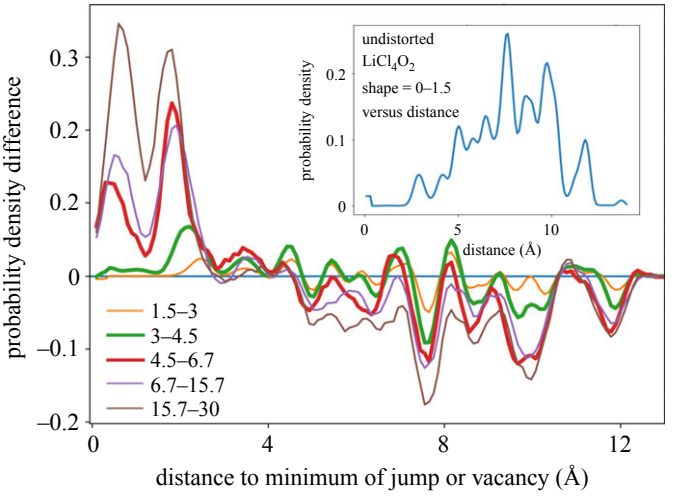

Figure 6. Probability distribution of minimum distances to the nearest vacancy or jumping Li^+, shown as a function of CSM shape distortion for each local Cl_4O_2 octahedral environment. Values for different CSM shape distortion ranges are shown in different colours, with the data in the main plot presented as difference in probability density with respect to the low-distortion distribution in the inset. Data are from the 1 vacancy simulation at 1100 K. (Online version in colour.)

shape versus minimum distance is provided in the electronic supplementary material, along with plots analogous to figure 5*a* for our other simulations.

The inset of figure 6 shows that least distorted octahedral environments (CSM values 0–1.5) occur at regular distances corresponding to the Wyckoff positions, with a maximum distance around 7 Å. The distributions for CSM values up to three show similar behaviour. However, as distortion increases, the correlation between shape and proximity to a vacancy or jump becomes

stronger. Probability density is removed from the mid-range distances and added to the two peaks around 1 and 2 Å, which are both closer than the nearest-neighbour Li Wyckoff position at 2.8 Å. Li^+ with CSM shape distortions larger than 6.7 are actively jumping (figure 5*a*) and are concentrated within 2.8 Å distances.

The most interesting insights can be obtained by focusing on Li^+ with CSM shape distortions in the tail of the main peak distribution in figure 5*a*, with CSM values between 3 and 6.7. Figure 6 shows that in this range, the distance histograms (bold green and red lines in figure 6) rapidly transition between a distribution with characteristics of the reference low-distortion case to a distribution that more closely mirrors actively jumping Li^+ (the high-distortion case). We may therefore infer that these intermediate distortions represent jump attempts or are actively starting or ending a jump. An additional plot of CSM shape evolution versus time for specific example jump event in the electronic supplementary material further illustrate this connection.

Notably, while it is established that increased thermal energy leads to faster diffusion, the temperature dependence of the CSM distortion distributions indicate that thermal oscillations also lead to a larger degree of local lattice distortion, which in turn is associated with more frequent jump attempts. In this respect, vacancies and thermal distortions act analogously. Similarly, the increased shape distortions of Li^+ neighbours to vacancies and jumping Li^+ may also indicate a softening of the lattice, which can further promote diffusion. In the electronic supplementary material, we show that with increased vacancy concentrations, we do observe a slight red shift in the temperature-dependent power spectrum. Indeed, previous studies have demonstrated the correlation between soft lattice modes and fast ionic diffusion [45,46]. The magnitude of the softening is relatively small, leading us to conclude that the local shape distortion is the more dominant dynamical effect and nuanced analyses at the atomic scale are illuminating.

(e) Additional vacancy-induced diffusion mechanisms

In addition to promoting additional jump attempts that raise the diffusion coefficient, vacancy-induced lattice distortion can also lead to additional diffusion mechanisms. In particular, we identify two additional diffusion mechanisms besides the dominant vacancy mediated diffusion mechanism in our simulations between 1100 and 1500 K. Although vacancy diffusion remains the primary mechanism, these two additional mechanisms play an increasingly important role as vacancy concentration (or temperature) is increased. Both mechanisms are prompted by the creation of a short-lived point defect; in particular, they start with an additional vacancy and self-interstitial pair and end with the annihilation of the self-interstitial. We distinguish between these two mechanisms here:

1. *The dumbbell-like or knock-off mechanism*. This mechanism involves concerted dynamics of two Li ions. An Li^+ jumps into an already occupied Li^+ site, creating a self-interstitial dumbbell. If the first jump then pushes its neighbour into a nearby vacancy, we label this paired jump process a knock-off defect. Literature calculations show that the knock-off mechanism has a slightly lower activation energy than the vacancy mediated diffusion, but requires the dominant charge carrier to be an Li-interstitial [11,12,14,16,40]. We are borrowing the term knock-off to describe a similar process in our simulations, although we assume Li vacancies to be the dominant charge carrier.
2. *The short-lived Frenkel defect mechanism*. This mechanism features Li-interstitials and vacancies that involve three or more jumps. We shall henceforth simply call these 's-Frenkel defects'. After the initial s-Frenkel interstitial and vacancy pair is created, Li^+ can jump into the new vacancy (labelled 'extra jump') or the interstitial can push an Li out of its site (labelled a 'push').

We used our jump tracking algorithm to categorize and track these additional diffusion mechanisms (see §2). We keep track of jumps outside of the vacancy-mediated diffusion

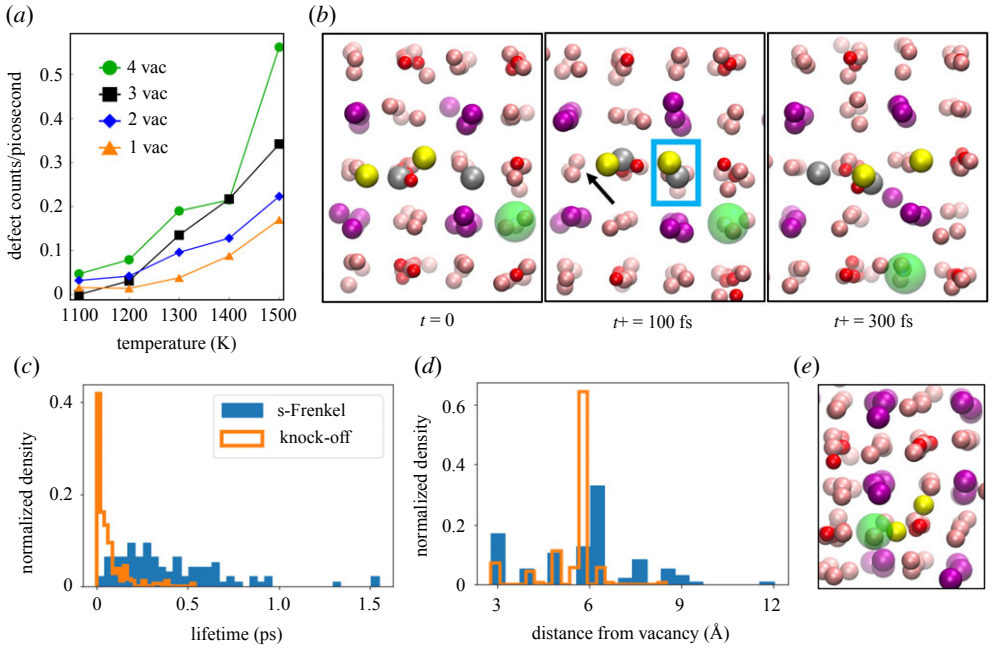

Figure 7. (*a*) Additional diffusion mechanisms (defects) are more common as temperature and the vacancy concentration increase. b. An example s-Frenkel mechanism from the 1 vacancy simulation at 1100 K has a life-time of approximately 300 fs and involves four additional jumps (yellow and grey Li). The blue box indicates the Li interstitial, the black arrow points at the new vacancy, and the green sphere is the native vacancy location. The distributions from all simulations of (*c*) life-time and (*d*) distance from the vacancy highlights differences between knock-off (orange) and s-Frenkel (blue) mechanisms. (*e*) The dumbbell shape of the knock-off mechanism is captured by two Li that sharing a site (yellow). (Online version in colour.)

mechanisms in a (python) dictionary and designate them a new jump, an extra jump, or a push by associating each jump with the initial self-interstitial creation. This dictionary is used to distinguish between the s-Frenkel and knock-off mechanisms by tracking the number of jumps before annihilation. We emphasize that most Li^+ jump into a vacant site, as expected. However, the additional s-Frenkel and knock-off mechanisms become more prevalent with temperature and vacancy concentration, representing up to 15% of the total jump events. This trend is evidenced in figure 7*a*, which tracks the increase in the prevalence of the self-interstitial 'defects' responsible for the two alternative diffusion mechanisms as a function of temperature and vacancy concentration.

For the dumbbell/knock-off mechanism, the time between the first jump (the formation of a vacancy and interstitial) and the second jump of the new interstitial into a vacancy site ranges from under 10 fs (nearly simultaneous) to over 540 fs (from the four vacancy simulation at 1200 K). The distribution of lifetimes is given in figure 7*c*. The average time between the two jumps over all simulations is 60 fs.

Compared with the dumbbell/knock-off mechanism, the s-Frenkel mechanism tends to feature longer-lived self-interstitial point defects, lasting up to 1550 fs (1 V'_{Li} 1500 K). Longer-lived defects are also more likely to occur in the lower vacancy concentration simulations because the interstitial is less likely to be annihilated by combining with a vacancy. The distribution of s-Frenkel lifetimes is given in figure 7*c*. and the average lifetime from all the simulations is 400 fs. We also find that s-Frenkel jumps can be highly correlated. For instance, the maximum number of jumps we recorded associated with a single s-Frenkel defect was 17 (2 V'_{Li} 1400 K), and the average number of jumps was 4. Our simulations show that the s-Frenkel defect can be annihilated either by combining with its own created vacancy or by combining with a nearby native vacancy, although we do not distinguish between these scenarios in our statistical analyses. Examples from individual simulations are highlighted below.

An example of an s-Frenkel defect involving four additional jumps from the 1 V'_{Li} simulation at 1100 K is shown in figure 7*b*. This s-Frenkel defect self-annihilates. The native vacancy, initiated at the beginning of the simulation and highlighted in green, is close to the self-interstitial creation site, but is not involved and diffuses once to a new site over the 300 fs lifetime of the s-Frenkel defect. The vacancy is created when Li^+ (yellow atom on the left) jumps and simultaneously pushes another Li^+ away (yellow atom on the right). The Li^+ interstitial (blue box) sits two sites away from the s-Frenkel vacancy. Then other Li^+ neighbours (grey) are pushed to the left of the frame, and one annihilates the s-Frenkel vacancy.

An example of a common knock-off mechanism can be illustrated using figure 2*b* and considering the sites labelled Li, 4NN, and an asterisk in a linear arrangement. Imagine that the vacancy is at the site labelled 4NN. The self-interstitial initiates at the site labelled Li and jumps into the occupied site, pushing that asterisk Li into the vacancy site labelled 4NN. These sites are 5.8 Å apart, a common distance for knock-off mechanisms to initiate with respect to the vacancy location. Figure 7*e* demonstrates a frame with the dumbbell shape from a knock-off mechanism that lasted 40 fs in the 1 V'_{Li} 1300 K simulation.

The results of our analyses of these two new mechanisms show that they often initiate close to native vacancy sites, indicating that the vacancies can induce the additional diffusion mechanisms. Figure 7*d* shows the distribution of distances from the native vacancy of the initial self-interstitial formation. Knock-off defects that are formed farther than 7 Å away from the vacancy are the result of the vacancy diffusing towards the defect. More s-Frenkel defects are formed further from the native vacancies, showing that vacancies themselves are not the only source of the additional diffusion mechanisms; rather, increased vacancy concentration apparently acts in concert with increased temperature. This interplay between temperature and vacancy concentration in promoting local lattice distortion has already been mentioned and appears to also play out in the initiation of the two secondary diffusion mechanisms. The contribution of these mechanisms rises with temperature, as more thermal energy is available to form the defects and the distortion around the vacancies increases.

We note that the knock-off mechanism is especially related to the vacancy mediated diffusion when the lifetime of the defect is short. Consider when two Li^+ jump within 10–50 of each other, it is difficult to determine which Li^+ *really* jumped first because jumps often take around 30–50 fs to complete (from the shape distortion analyses). Since 58% of knock-off jumps occur within 50 fs of each other, these jumps could also be simply described as highly correlated jumps in space *and time*, as we describe in §3f.

In summary, the initial proximity of the self-interstitials to native vacancies, combined with the increased probability of forming self-interstitials (figure 7*a*) at higher vacancy concentrations, lead us to conclude that vacancies increase jump attempts within the two alternative dumbbell/knock-off and s-Frenkel mechanisms. The probability of these mechanisms also increases with temperature *faster* for simulations with increased vacancy concentrations. Consequently, the higher D_0 of the four and three vacancy simulations may be in part due to the increased prevalence of the two new diffusion mechanisms, in addition to the higher frequency of jump attempts due to the vacancy-induced distortions. The knock-off mechanism potentially has a lower activation energy barrier than the vacancy-mediated mechanism, which may help to explain the lower activation energy barrier at these concentrations. Together, we speculate that these factors contribute to the non-Arrhenius behaviour of the simulations with one to three vacancies. Note also that significant increases in probability for the two alternative mechanism occur at different temperatures depending on the vacancy concentration, with higher concentrations favouring increases starting at lower temperatures. These changes roughly correlate with the onset of non-Arrhenius behaviour from figure 1. In §3f, we will explore correlated jumps between interacting vacancies and provide additional evidence of the importance of spatio-temporal locality in the jump mechanism.

(f) Additional evidence for spatiotemporal jump correlation

Correlated motion is a common factor that increases diffusivity in many of the promising superionic materials, such as $Li_{10}GeP_2S_{12}$ (LGPS) and $Li_7La_3Zr_2O_{12}$ [47] (LLZO), which have intrinsic vacancies and high concentrations of diffusive charge carriers. A correlation descriptor that could predict beneficial correlated motion would help the discovery of new solid-electrolyte materials; however, the effect of correlated motion on the diffusion mechanism is specific to each material. For example, correlated motion of Li^+ in LGPS and LLZO can extend over distances equal to many lattice vectors along diffusion channels [47]. In contrast, Li_3OCl lacks defined diffusion channels and features relatively low concentrations of V'_{Li} charge carriers. Accordingly, correlated motion in Li_3OCl happens over much shorter distances and times; nevertheless, such correlation is still a critical component of the diffusion mechanisms.

Our results provide strong evidence that correlated motion is beneficial to diffusivity in Li_3OCl through the lowering of the activation energy barrier and promoting jumps in the *same* direction. There are two common methods to demonstrate correlated motion: the Haven ratio, H_r, and the distinct van Hove correlation function (figure 8). H_r accounts for the effect of correlated motion on conductivity, σ, compared to the self-diffusivity, D, through the Nernst–Einstein relationship

$$\frac{\sigma}{D} = \frac{nq^2}{kT} H_r, \tag{3.1}$$

where the previously undefined variables are n, the nominal density of mobile ions, and q, the charge of the mobile ion. The self-diffusivity can be experimentally determined by isotopically labelling a few mobile ions and measuring the tracer diffusion coefficient, D^*. It is then straightforward to obtain the Haven ratio through $H_r = D^*/D_\sigma$, where D_σ is derived from the Nernst-Einstein relationship after experimentally measuring σ. If D_σ is larger than the tracer diffusivity, then $H_r < 1$, indicating beneficial correlated motion.

Now consider that D_σ increases with n, but the self-diffusivity will not necessarily increase because it is derived from the average MSD of all the mobile species:

$$D = \frac{1}{6N\Delta t} \sum_{i=1}^{N} \langle |\mathbf{r}_i(t + \Delta t) - \mathbf{r}_i t|^2 \rangle_t. \tag{3.2}$$

For many materials, this distinction is vital. For instance, D depends significantly on $C(V'_{Li})$ in Li_3OCl due to the vacancy-mediated mechanism.

Computational studies have estimated H_r through a number of methods [48], but the most common approximation involves just setting $H_r = 1$, which denotes uncorrelated motion or the dilute concentration limit. However, superionic materials are often far from the dilute limit, questioning this approach. More accurate methods estimate the conductivity through the change in the mobile ion charge density (or centre of mass). This method was used to show $H_r < 1$ for Li_2HOCl [19], AgI [49] and $Li_{10}GeP_2S_{12}$ [50]. In another method, H_r is set equal to a 'thermodynamic factor', Γ^{-1}. The inverse, Γ, is then evaluated by averaging the fluctuations in site occupation over the simulation [51]; using this approach, Γ^{-1} was found to be much less than 1 for $Li_5La_3Ta_2O_{12}$ [52].

In this work, we choose not to estimate H_r using the methods mentioned above because they require robust statistics and thus very long simulations and large system sizes to converge D_σ. However, in the electronic supplementary material, we present a simple method to estimate correlated motion in the case of vacancy diffusion, which indicates correlated motion in the $1V'_{Li}$ is minimal compared to higher vacancy concentrations. In addition, we quantify the correlation between vacancies using other methods as described below, including incorporating a novel spatio-temporal jump correlation analysis and comparing the angle between jumps. We point out that correlation behaviour in superionic materials has also been estimated in several additional ways by other researchers [38,53,54].

We first introduce a novel jump correlation spatio-temporal analysis. This analysis is very similar to the distinct Van–Hove correlation function [55], $G_d(r, t)$, which tracks changes in the

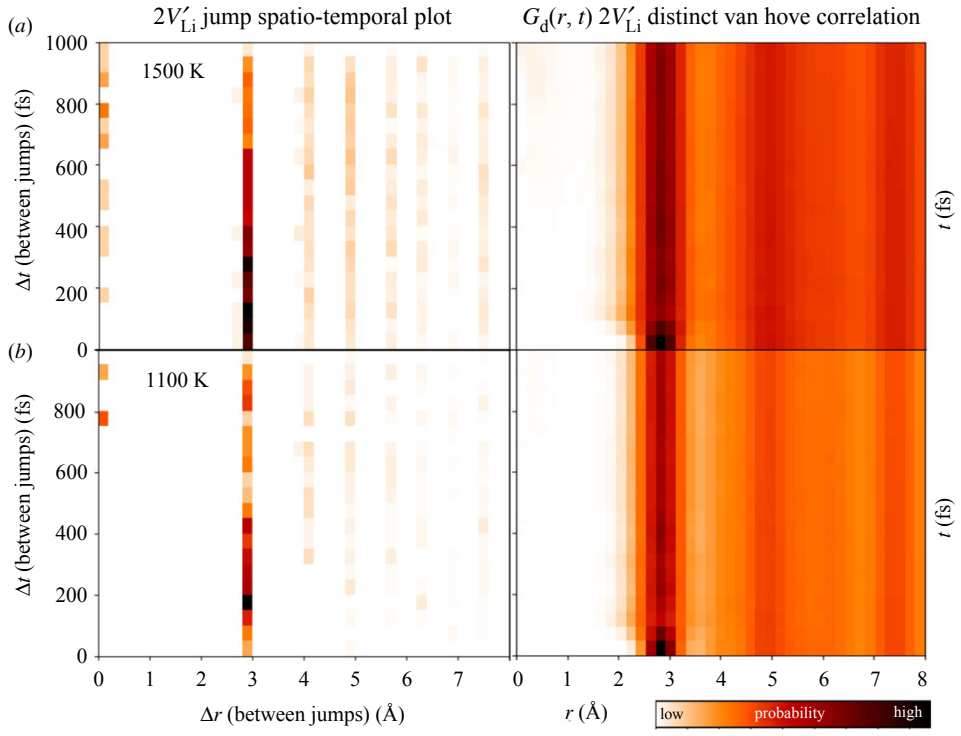

Figure 8. (*a*) Jump correlation spatio-temporal plot for $2V'_{Li}$ at 1500 K and (*b*) at 1100 K (left panels). The probability of finding two jumps starting from a distance Δr apart is normalized by the solid angle shell. The distinct Van Hove Correlation functions, $G_d(r, t)$, hint at some correlated motion and indicate a similar time between jumps (right panels). (Online version in colour.)

pair distribution function of distinct atoms over time. However, instead of tracking the distance of all Li^+, we confine our analysis to only track those Li^+ that jump. Specifically, we plot Δt, the time between jumps, versus Δr, the distance between jumps. Figure 8 shows the jump spatio-temporal plot for the 2 V'_{Li} simulation at (*a*) 1500 and (*b*) 1100 K and the comparative $G_d(r, t)$ (other temperatures and vacancy concentrations are given in the electronic supplementary material). These plots convey the probability that one jump will follow another. The probability that correlated jumps occur is highly sensitive to the time and distance cutoff, which is displayed simultaneously in the spatio-temporal plot. The probability is normalized with respect to the density of sites within a volume slice $r + dr$ at a given distance r. We also remove back-jumps if they occur within 500 fs. A time cutoff for visualizing correlation was set to 1000 fs, as is standard in plots of $G_d(r, t)$; thus, all jumps that occur within 1000 fs of each other are accounted for in the analyses.

The first evidence of correlated motion is the high probability of two jumps occurring within 300 fs. Figure 8*b* shows the high probability as the black square at 2.8 Å and 150 fs. At 1100 K, the most probable time between jumps is approximately 150 fs, which is much smaller than the *expected* time between random jumps of 770 fs. This expected time is computed from a Poisson distribution of random Markovian jumps based on the total number of jumps that occur in the simulation time. Thus, we see that jumps are correlated rather than random, and are clustered in time and space. Even at 1500 K, when the expected time between random jumps drops to 340 fs, the most probable time between jumps drops to much lower than 100 fs.

The most probable distance between jumps are those starting from first nearest-neighbour positions (1NN) at 2.8 Å. There are two possible scenarios that lead to 1NN jumps: (i) an Li^+ jumps, leaving behind a vacancy, and its 1NN immediately jumps into the new vacancy location, as shown by the black and grey arrows in figure 2*b* and (ii) two vacancies are close to one

another, such that 1NN Li^+ then jump into those separate vacancies (leaving the vacancies as first nearest neighbours), as shown by the black and red arrows in figure 2. We know that in the 2 V'_{Li} simulation there is a high probability of finding vacancies as nearest neighbours (figure 3), so the second scenario is possible, but the first scenario is far more likely. In fact, the electronic supplementary material shows that with 1 V'_{Li}, there still exists a high probability of finding 1NN subsequent jumps between 100 and 200 fs at 1100 K, which can only be justified according to the first scenario. We refer to these clusters of jumps in space and time as 'hot zones', where the balance of enthalpy and entropy at a given temperature transfers to the entropic regime and many jump events occur [56]. The s-Frenkel mechanism is also an example of an entropic 'hot zone'.

The second evidence of correlated motion lies in the isolated high probabilities of jumps occurring at $\Delta r = 4.9$ Å (3NN) and $\Delta t = 225$ fs, and at $\Delta r = 6.3$ Å (5NN) and $\Delta t = 200$ fs in the 2 V'_{Li} 1100 K simulation. These isolated islands of higher probability are evidence of the hot zone, where jumps are clustered in space and time. Note that there is no probability of jumps at a distance of 4 Å until 375 fs, likely due to the low probability of finding V'_{Li} at that distance and the need to overcome a binding barrier for closely spaced vacancies (figure 2). Interestingly, once kB T increases in the 1500 K simulation, jumps occur 4 Å apart at any time interval. Further, spatio-temporal plots given in the electronic supplementary material show that the probability of finding jumps *correlated in time* and 4 Å apart is less likely than the other near-neighbour distances at 1100 K for all the multi-V'_{Li} simulations. As the vacancies increase to 3 and 4, the probability of finding two jumps within 100 fs increases at all the distances plotted, including at 4 Å. In summary, correlated jumps at low temperatures are evident from the higher probabilities of jumps occurring close in time and at close distances, especially 1NN/3NN/5NN. The spatio-temporal jump correlation plots provide information on correlation beyond the distinct van Hove correlation function analyses and can also be used to understand superionic materials with other diffusion mechanisms.

The spatio-temporal plots demonstrate that correlated jumps occur, but not if their velocity or direction is correlated. We find correlated motion in the same direction, which will increase diffusivity compared to correlated motion in opposing directions. The repulsion between vacancies can act to beneficially push one ahead of the other, leading to vacancies jumping in a similar forward direction. This effect can be quantified by calculating the angle between jumps i and j, $\theta_{i,j}$, as a measure of short-range correlated motion. Henceforth, we define $\theta_{i,j}$ as the two-jump angle. This metric is inspired by the Bardeen–Herring correlation factor, which equals the Haven ratio for vacancy-mediated diffusion assuming no vacancy interaction [48,57]; however, our metric has an advantage in that it is appropriate for interacting vacancies like those found in Li_3OCl.

For our analysis, we select only jumps that occur within reasonable time and distance cutoffs, as chosen from the spatio-temporal plots. In figure 9*a*,*b*, we set distance and time cutoffs at $\Delta r = 6.4$ Å and $\Delta t = 600$ fs, which captures correlated jumps that occur within 5NN at 1100 K. We explore the sensitivity of our analyses to the cutoffs by comparing histograms of the two jump angles. We show the 2 V'_{Li} simulations at 1100 and 1500 K in the main text to isolate the interaction between just two vacancies. The electronic supplementary material shows the other concentrations and a larger time cutoff of 1600 fs.

Correlated motion in the same direction is demonstrated by sensitivity of the histogram to the distance cutoff, especially if set to only capture jumps starting at 1NN and 2NN (blue and orange in the histogram). Jumps in exactly the same direction (0°) are more common with a cutoff of 4.3 Å than with a larger distance cutoff. This trend holds at higher temperatures and $C(V'_{Li})$, except for the $1V'_{Li}$ simulations at 1100 K.

Our jump correlation script filters out back-jumps, where an Li jump from site a to b and back to a, within 500 fs. The filter lowers the probability of finding $\theta_{i,j} = 180°$. However, some back-jumps do occur, especially at the maximum time cutoff is 1600 fs. In addition, for the simulations with multiple vacancies, jumps associated with different vacancies can result in $\theta_{i,j} = 180°$.

Another indication of correlated motion can be found in the ratio of $\theta_{i,j} = 90°$ to 120°. Within the 600 fs time cutoff and temperatures = 1100–1200 K, the probability of finding $\theta_{i,j} = 120°$ is

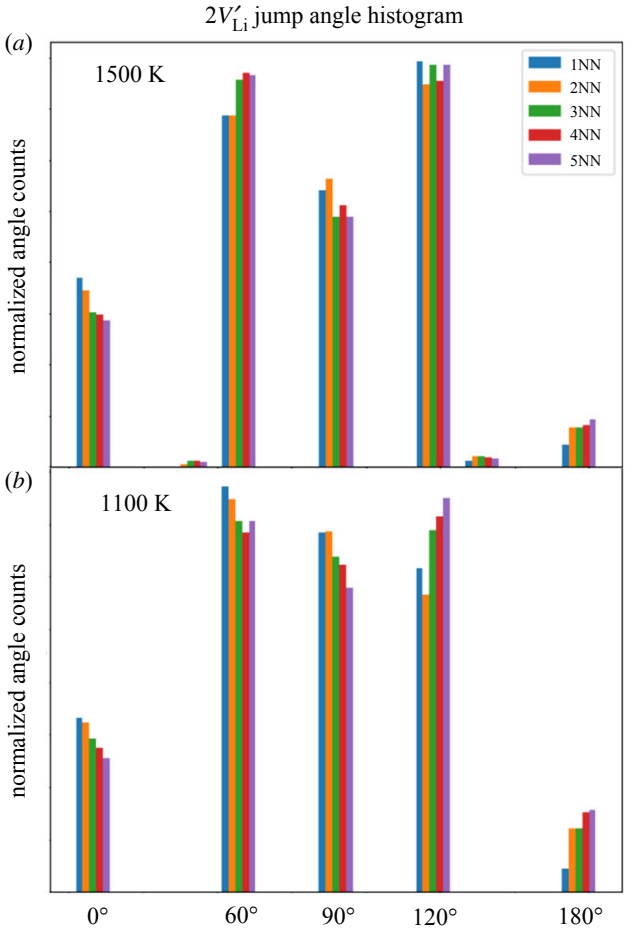

Figure 9. From the $2V'_{Li}$ simulation, the histogram of the angle between two jumps with time cutoff of 600 fs shows rarer angles of 45° and 135° at (*a*) 1500 K and strong dependence on the distance cutoff at (*b*) 1100 K. (Online version in colour.)

similar to $\theta_{i,j} = 90°$. As temperature increases, more jumps in opposing directions are found with $\theta_{i,j} = 120°$ or 180°. At the maximum time cutoff of 1600 fs, all the distributions look similar (see electronic supplementary material), with similar probability that the two jump angle equals 60° and 120° and a lower probability of a 90°. In addition, at higher temperatures 45°and 135° angles appear, for all vacancy concentrations, in addition to the 0°, 60°, 90°, 120° and 180° observed at all temperatures.

In summary, we can extract three key indicators of correlated motion from the two jump angle histograms: (i) beneficial correlated motion (not in opposing directions) is more probable for nearest or next nearest Li in the multi-vacancy simulations. (ii) Correlated jumps in the same direction (or at 90°) are found especially at lower temperatures and with a more strict time cutoff of approximately 600 fs versus 1600 fs. High temperatures wash out some of the effects of V'_{Li} interaction on correlated jumps. (iii) Less correlated motion is observed in the 1 V'_{Li} simulation, and no obvious trends are observed that suggest more correlated motion for a particular simulation with multiple V'_{Li}.

4. Conclusion

Through comparing simulations at increasing V'_{Li} concentrations in Li_3OCl, we find that analysing the effect of vacancies on their local environment sheds light on the

non-Arrhenius behaviour and lower activation energy barrier of simulations with 1.5–2% vacancy concentrations. The vacancies affect the lattice through local strain and polarization of neighbouring ions. The local strain distorts the octahedral environment of Li^+ close to the vacancy and induces jump attempts, including jumps that lead to additional diffusion mechanisms outside the dominant vacancy-mediated mechanism. At higher vacancy concentrations, the close proximity of many V'_{Li} enhances the lattice distortion, which promotes cascades of correlated diffusion events. The additional diffusion mechanisms and evidence of correlation motion were revealed through novel analyses of discrete vacancy diffusion events. In addition, vacancy–vacancy interactions were shown through detailed energetic, structural, and dynamic analyses.

We note that it is difficult to synthesize H-free Li_3OCl and thus directly compare our computational results to experiment [9], which feature a range of E_a values spanning 0.25–1.1 eV. Furthermore, lithium hydroxychloride shows almost an order of magnitude difference in conductivity between the 10% proton 'doped' and 20% (and above) doped anti-perovskites [17,20]. However, the activation energies at different doping levels are similar, so the effect must be from higher concentrations of charge carriers and potentially a higher jump attempt frequency. At low proton concentrations in $Li_{3-x}OH_xCl$, the *mechanism* is still vacancy mediated and most jumps do not involve interactions with protons. Accordingly, our results regarding the importance of the vacancy's local distortions and correlated motion should map onto experimental realities, with qualitative applicability across a wide range of compositions.

Data accessibility. The simulations analysed in this article are provided through Dryad: https://doi.org/10.5061/dryad.jsxksn08j.

Authors' contributions. Z.M. is first author. N.A. is corresponding author. All other authors contributed to the data and writing.

Competing interests. The authors report no competing interests.

Funding. The work performed at SFSU and by Z. Mehmedović[1] while at SFSU was supported by the National Science Foundation under grant no. DMR-1710630 and simulations utilized the Extreme Science and Engineering Discovery Environment (XSEDE) Stampede2 at the University of Texas, Austin through allocation DMR180033. The work by P. Shea and B. C. Wood was performed under the auspices of the U.S. Department of Energy by Lawrence Livermore National Laboratory under Contract DE-AC52-07NA27344. The authors acknowledge financial support from the US Department of Energy (DOE), Office of Energy Efficiency and Renewable Energy, Vehicle Technologies Office, through the Battery Materials Research program.

Acknowledgements. Thanks to Shannon R. McCurdy for statistical advice, to Stephen Weitzner for his help with the phonon spectra, and to Leonid Kahle and Alby Musaelian for help with Sitator.

References

1. Bachman JC *et al.* 2016 Inorganic solid-state electrolytes for lithium batteries: mechanisms and properties governing ion conduction. *Chem. Rev.* **116**, 140–162. (doi:10.1021/acs.chemrev.5b00563)
2. McCloskey BD. 2015 Attainable gravimetric and volumetric energy density of Li-S and Li Ion battery cells with solid separator-protected Li metal anodes. *J. Phys. Chem. Lett.* **6**, 4581–4588. (doi:PMID: 26722800.)
3. Kerman K, Luntz A, Viswanathan V, Chiang YM, Chen Z. 2017 Practical challenges hindering the development of solid state Li ion batteries. *J. Electrochem. Soc.* **164**, A1731–A1744. (doi:10.1149/2.1571707jes)
4. Lin YY, Bin Yong AX, Gustafson WJ, Reedy CN, Ertekin E, Krogstad JA, Perry NH. 2020 Toward design of cation transport in solid-state battery electrolytes: structure-dynamics relationships. *Curr. Opin. Solid State Mater. Sci.* **24**, 100875. (doi:10.1016/j.cossms.2020.100875)
5. Tong Z, Wang SB, Liao YK, Hu SF, Liu RS. 2020 Interface between solid-state electrolytes and Li-Metal anodes: issues, materials, and processing routes. *ACS Appl. Mater. Interfaces* **12**, 47 181–47 196. (doi:10.1021/acsami.0c13591)
6. Wang S, Bai Q, Nolan AM, Liu Y, Gong S, Sun Q, Mo Y. 2019 Lithium chlorides and bromides as promising solid-state chemistries for fast ion conductors with good electrochemical stability. *Angew. Chem. Int. Ed.* **58**, 8039–8043. (doi:10.1002/anie.201901938)

7. Gao Z, Sun H, Fu L, Ye F, Zhang Y, Luo W, Huang Y. 2018 Promises, challenges, and recent progress of inorganic solid-state electrolytes for all-solid-state Lithium batteries. *Adv. Mater.* **22**, 1 705 702–1 705 727. (doi:10.1002/adma.201705702)
8. Randau S *et al.* 2020 Benchmarking the performance of all-solid-state lithium batteries. *Nat. Energy* **5**, 259–270.
9. Hanghofer I, Redhammer GJ, Rohde S, Hanzu I, Senyshyn A, Wilkening HMR, Rettenwander D. 2018 Untangling the structure and dynamics of Lithium-Rich anti-perovskites envisaged as solid electrolytes for batteries. *Chem. Mater.* **30**, 8134–8144. (doi:10.1021/acs.chemmater.8b02568)
10. Luntz AC, Voss J, Reuter K. 2015 Interfacial challenges in solid-state Li Ion batteries. *J. Phys. Chem. Lett.* **6**, 4599–4604. (doi:10.1021/acs.jpclett.5b02352)
11. Wu M, Xu B, Lei X, Huang K, Ouyang C. 2018 Bulk properties and transport mechanisms of a solid state antiperovskite Li-ion conductor Li_3OCl: insights from first principles calculations. *J. Mater. Chem. A* **6**, 1150–1160. (doi:10.1039/C7TA08780B)
12. Lu Z, Chen C, Baiyee ZM, Chen X, Niu C, Ciucci F. 2015 Defect chemistry and lithium transport in Li_3OCl anti-perovskite superionic conductors. *Phys. Chem. Chem. Phys.* **17**, 32 547–32 555. (doi:10.1039/C5CP05722A)
13. Zhang Y, Zhao Y, Chen C. 2013 Ab initio study of the stabilities of and mechanism of superionic transport in Lithium-rich antiperovskites. *Phys. Rev. B* **87**, 134303. (doi:10.1103/PhysRevB.87.134303)
14. Emly A, Kioupakis E, Van der Ven A. 2013 Phase stability and transport mechanisms in antiperovskite Li_3OCl and Li_3OBr superionic conductors. *Chem. Mater.* **25**, 4663–4670. (doi:10.1021/cm4016222)
15. Zhao Y, Daemen LL. 2012 Superionic conductivity in lithium-rich anti-perovskites. *J. Am. Chem. Soc.* **134**, 15 042–15 047. (doi:PMID: 22849550.)
16. Stegmaier S, Voss J, Reuter K, Luntz AC. 2017 Li^+ defects in a solid-state Li ion battery: theoretical insights with a Li_3OCl electrolyte. *Chem. Mater.* **29**, 4330–4340. (doi:10.1021/acs.chemmater.7b00659)
17. Song AY *et al.* 2018 Protons enhance conductivities in lithium halide hydroxide/lithium oxyhalide solid electrolytes by forming rotating hydroxy groups. *Adv. Energy Mater.* **8**, 1700971. (doi:10.1002/aenm.201700971)
18. Howard J, Hood ZD, Holzwarth NAW. 2017 Fundamental aspects of the structural and electrolyte properties of Li_2OHCl from simulations and experiment. *Phys. Rev. Mater.* **1**, 075406. (doi:10.1103/PhysRevMaterials.1.075406)
19. Howard JD, Holzwarth N. 2018 Analysis of the statistical and convergence properties of ionic transport coefficients with application to the solid electrolyte Li_2OHCl. *Solid State Ionics* **325**, 80–89. (doi:10.1016/j.ssi.2018.07.025)
20. Dawson JA, Attari TS, Chen H, Emge SP, Johnston KE, Islam MS. 2018 Elucidating lithium-ion and proton dynamics in anti-perovskite solid electrolytes. *Energy Environ. Sci.* **11**, 2993–3002. (doi:10.1039/C8EE00779A)
21. Marx D, Hutter J. 2000 Ab initio molecular dynamics: theory and implementation. In *Modern methods and algorithms of quantum chemistry* (ed. J Grotendorst), pp. 301–449, vol. 1. Jülich, Germany: John von Neumann Institute for Computing.
22. Kohn W, Sham LJ. 1965 Self-consistent equations including exchange and correlation effects. *Phys. Rev.* **140**, A1133–A1138. (doi:10.1103/PhysRev.140.A1133)
23. Hafner J. 2008 Ab-initio simulations of materials using VASP: density-functional theory and beyond. *J. Comput. Chem.* **29**, 2044–2078. (doi:10.1002/jcc.21057)
24. Kresse G, Furthmüller J. 1996 Efficient iterative schemes for ab initio total-energy calculations using a plane-wave basis set. *Phys. Rev. B* **54**, 11 169–11 186. (doi:10.1103/PhysRevB.54.11169)
25. Blöchl PE. 1994 Projector augmented-wave method. *Phys. Rev. B* **50**, 17 953–17 979. (doi:10.1103/PhysRevB.50.17953)
26. Kresse G, Joubert D. 1999 From ultrasoft pseudopotentials to the projector augmented-wave method. *Phys. Rev. B* **59**, 1758–1775. (doi:10.1103/PhysRevB.59.1758)
27. Perdew JP, Burke K, Ernzerhof M. 1996 Generalized gradient approximation made simple. *Phys. Rev. Lett.* **77**, 3865. (doi:10.1103/PhysRevLett.77.3865)

28. Chen MH, Emly A, Van der Ven A. 2015 Anharmonicity and phase stability of antiperovskite Li_3OCl. *Phys. Rev. B* **91**, 214306. (doi:10.1103/PhysRevB.91.214306)
29. Henkelman G, Uberuaga BP, Jansson H. 2000 A climbing image nudged elastic band method for finding saddle points and minimum energy paths. *J. Chem. Phys.* **113**, 9901–9904. (doi:10.1063/1.1329672)
30. Kahle L, Musaelian A, Marzari N, Kozinsky B. 2019 Unsupervised landmark analysis for jump detection in molecular dynamics simulations. (http://arxiv.org/abs/1902.02107)
31. Marzari N, Mostofi AA, Yates JR, Souza I, Vanderbilt D. 2012 Maximally localized Wannier functions: theory and applications. *Rev. Mod. Phys.* **84**, 1419–1475. (doi:10.1103/RevModPhys.84.1419)
32. Wang Z, Xu H, Xuan M, Shao G. 2017 From anti-perovskite to double anti-perovskite: tuning lattice chemistry to achieve super-fast Li^+ transport in cubic solid lithium halogen–chalcogenides. *J. Mater. Chem. A* **6**, 73–83. (doi:10.1039/C7TA08698A)
33. Dawson JA, Chen H, Islam MS. 2018 Composition screening of Lithium-and sodium-rich anti-perovskites for fast-conducting solid electrolytes. *J. Phys. Chem. C* **122**, 23 978–23 984. (doi:10.1021/acs.jpcc.8b08208)
34. Dawson JA, Canepa P, Famprikis T, Masquelier C, Islam MS. 2017 Atomic-scale influence of grain boundaries on Li-Ion conduction in solid electrolytes for all-solid-state batteries. *J. Am. Chem. Soc.* **140**, 362–368. (doi:10.1021/jacs.7b10593)
35. Chen B, Xu C, Zhou J. 2018 Insights into grain boundary in Lithium-rich anti-perovskite as solid electrolytes. *J. Electrochem. Soc.* **165**, A3946–A3951. (doi:10.1149/2.0831816jes)
36. Shen K, Wang Y, Zhang J, Zong Y, Li G, Zhao C, Chen H. 2020 Revealing the effect of grain boundary segregation on Li ion transport in polycrystalline anti-perovskite Li_3ClO: a phase field study. *Phys. Chem. Chem. Phys.* **22**, 3030–3036. (doi:10.1039/C9CP06055C)
37. Ngai K. 1998 Meyer–Neldel rule and anti Meyer–Neldel rule of ionic conductivity: conclusions from the coupling model. *Solid State Ionics* **105**, 231–235. (doi:10.1016/S0167-2738(97)00469-4)
38. Heenen HH, Voss J, Scheurer C, Reuter K, Luntz AC. 2019 Multi-ion conduction in Li_3OCl glass electrolytes. *J. Phys. Chem. Lett.* **10**, 2264–2269. (doi:10.1021/acs.jpclett.9b00500)
39. Deng Z, Radhakrishnan B, Ong SP. 2015 Rational composition optimization of the Lithium-Rich $Li_3OCl_{1-x}Br_x$ anti-perovskite superionic conductors. *Chem. Mater.* **27**, 3749–3755. (doi:10.1021/acs.chemmater.5b00988)
40. Mouta R, Melo MAB, Diniz EM, Paschoal CWA. 2014 Concentration of charge carriers, migration, and stability in Li_3OCl solid electrolytes. *Chem. Mater.* **26**, 7137–7144. (doi:10.1021/cm503717e)
41. Zevgolis A, Wood BC, Mehmedović Z, Hall AT, Alves TC, Adelstein N. 2018 Alloying effects on superionic conductivity in lithium indium halides for all-solid-state batteries. *APL Mater.* **6**, 047903. (doi:10.1063/1.5011378)
42. Adelstein N, Wood BC. 2016 Role of dynamically frustrated bond disorder in a Li^+ superionic solid electrolyte. *Chem. Mater.* **28**, 7218–7231. (doi:10.1021/acs.chemmater.6b00790)
43. Zabrodsky H, Peleg S, Avnir D. 2002 Continuous symmetry measures. *J. Am. Chem. Soc.* **114**, 7843–7851. (doi:10.1021/ja00046a033)
44. Llunell M, Casanova D, Cirera J, Bofill J, Alemany P, Alvarez S, Pinsky M, Avnir D. 2013 SHAPE v. 2.1. program for the calculation of continuous shape measures of polygonal and polyhedral molecular fragments.
45. Kraft MA *et al.* 2017 Influence of lattice polarizability on the ionic conductivity in the Lithium superionic argyrodites Li_6PS_5X (X = Cl, Br, I). *J. Am. Chem. Soc.* **139**, 10 909–10 918. (doi:10.1021/jacs.7b06327)
46. Muy S, Voss J, Schlem R, Koerver R, Sedlmaier SJ, Maglia F, Lamp P, Zeier WG, Shao-Horn Y. 2019 High-throughput screening of solid-state Li-Ion conductors using lattice-dynamics descriptors. *ISCIENCE* **16**, 270–282. (doi:10.1016/j.isci.2019.05.036)
47. He X, Zhu Y, Mo Y. 2017 Origin of fast ion diffusion in super-ionic conductors. *Nat. Commun.* **8**, 15893. (doi:10.1038/ncomms15893)
48. Murch G. 1982 Invited review: the haven ratio in fast ionic conductors. *Solid State Ionics* **7**, 177–198. (doi:10.1016/0167-2738(82)90050-9)

49. Morgan BJ, Madden PA. 2014 Relationships between atomic diffusion mechanisms and ensemble transport coefficients in crystalline polymorphs. *Phys. Rev. Lett.* **112**, 145901. (doi:10.1103/PhysRevLett.112.145901)
50. Marcolongo A, Marzari N. 2017 Ionic correlations and failure of Nernst-Einstein relation in solid-state electrolytes. *Phys. Rev. Mater.* **1**, 025402. (doi:10.1103/PhysRevMaterials.1.025402)
51. Klenk M, Lai W. 2015 Local structure and dynamics of lithium garnet ionic conductors: tetragonal and cubic $Li_7La_3Zr_2O_7$. *Phys. Chem. Chem. Phys.* **17**, 8758–8768. (doi:10.1039/C4CP05690F)
52. Wang Y, Klenk M, Page K, Lai W. 2014 Local structure and dynamics of lithium garnet ionic conductors: a model material $Li_5La_3Ta_2O_{12}$. *Chem. Mater.* **26**, 5613–5624. (doi:10.1021/cm502133c)
53. Morgan B. 2017 Lattice-geometry effects in garnet solid electrolytes: a lattice-gas Monte Carlo simulation study. *R. Soc. Open Sci.* **4**, 170824. (doi:10.1098/rsos.170824)
54. de Klerk NJ, van der Maas E, Wagemaker M. 2018 Analysis of diffusion in solid-state electrolytes through MD simulations, improvement of the Li-ion conductivity in β-Li_3PS_4 as an example. *ACS Appl. Energy Mater.* **1**, 3230–3242. (doi:10.1021/acsaem.8b00457)
55. Van Hove L. 1954 Correlations in space and time and born approximation scattering in systems of interacting particles. *Phys. Rev.* **95**, 249–262. (doi:10.1103/PhysRev.95.249)
56. Varley JB, Kweon K, Mehta P, Shea P, Heo TW, Udovic TJ, Stavila V, Wood BC. 2017 Understanding ionic conductivity trends in polyborane solid electrolytes from ab initio molecular dynamics. *ACS Energy Lett.* **2**, 250–255. (doi:10.1021/acsenergylett.6b00620)
57. Bardeen J, Herring C. 1952 Diffusion in alloys and the Kirkendall effect. In *Imperfections in nearly perfect crystals*, pp. 261–281. New York, NY: Wiley.